Research Article | Open Access

Greenverse Science

Wu *et al. Greenverse Sci.* **2026**, *1*, 19 **DOI:**10.20517/greenvsci.2026.24

Electronic structure modulation through superexchange in spinel oxides for simultaneous NO_x and propane removal

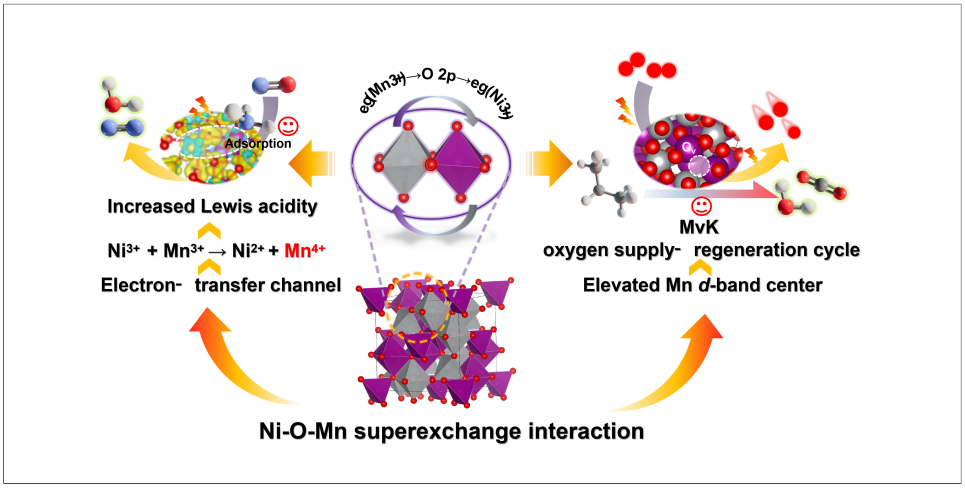
Jiahui Wu[1,2], Yaqin Hou[1,2,*], Shuang Ma[1,2], Yujing Han[1,2], Ke Liu[1,2], Yan Cui[1,2], Weiren Bao[3], Jiancheng Wang[4], Zhanggen Huang[1,2,*]

Keywords:
Superexchange interaction, NO_x reduction, propane oxidation, simultaneous removal, spinel oxides, electronic structure

Citation: Wu, J.; Hou, Y.; Ma, S.; Han, Y.; Liu, K.; Cui, Y.; Bao, W.; Wang, J.; Huang, Z. Electronic structure modulation through superexchange in spinel oxides for simultaneous NO_x and propane removal. *Greenverse Sci.* **2026**, *1*, 19. https://dx.doi.org/10.20517/greenvsci.2026.24

Received: 10 Sep 2026
First Decision: 10 Oct 2026
Revised: 6 Nov 2026
Accepted: 19 Nov 2026
Published: 26 Nov 2026

Academic Editor: Dengsong Zhang
Copy Editor: Tong Wang
Production Editor: Tong Wang



Abstract

The coexistence of nitrogen oxides (NO_x) and volatile organic compounds (VOCs) in industrial flue gases remains a significant challenge for air pollution control, necessitating the development of bifunctional catalysts capable of simultaneous removal. Herein, a series of Mn-based spinel catalysts was synthesized to investigate the role of A-O-Mn superexchange interactions in the simultaneous removal of NO_x and C_3H_8. These interactions modulated the electronic structure of the catalysts and were associated with improved overall catalytic performance. Among the investigated catalysts, $NiMn_2O_4$ exhibited the best performance, achieving 91.4% C_3H_8 conversion and 92.8% NO_x conversion simultaneously at 220 °C, along with the highest N_2 selectivity and satisfactory SO_2 resistance. Comprehensive experimental characterizations and density functional theory (DFT) calculations revealed that the superior catalytic performance originated from the Ni-O-Mn superexchange interaction. This interaction induced strong Ni_{oct}-O-Mn_{oct}

[1]State Key Laboratory of Coal Conversion, Institute of Coal Chemistry, Chinese Academy of Sciences, Taiyuan 030001, Shanxi, China.
[2]University of Chinese Academy of Sciences, Beijing 100049, China.
[3]State Key Laboratory of Clean and Efficient Utilization, College of Chemistry and Chemical Engineering, Taiyuan University of Technology, Taiyuan 030024, Shanxi, China.
[4]Shanxi Key Laboratory of Complex Air Pollution Control and Carbon Reduction, College of Environmental Science and Engineering, Taiyuan University of Technology, Taiyuan 030024, Shanxi, China.

[*]**Correspondence to:** Dr. Yaqin Hou, Prof. Zhanggen Huang, State Key Laboratory of Coal Conversion, Institute of Coal Chemistry, Chinese Academy of Sciences, Taiyuan 030001, Shanxi, China. E-mail: houyaqin@sxicc.ac.cn; zghuang@sxicc.ac.cn.

orbital connectivity, forming an efficient electron-transfer channel that stabilized surface Mn^{4+} species and enhanced Lewis acidity, thereby promoting the adsorption and activation of both NH_3 and C_3H_8. Concurrently, the superexchange significantly elevated the Mn d-band center, lowering the oxygen vacancy formation energy (1.368 eV) via efficient electron delocalization during oxygen cycling while establishing a highly efficient oxygen consumption-replenishment cycle that sustained the Mars-van Krevelen mechanism. This work provides mechanistic insights into A-O-Mn superexchange interactions in spinel lattices, offering theoretical insights for the rational design of high-performance catalysts for simultaneous removal.

INTRODUCTION

The coexistence of nitrogen oxides (NO_x) and volatile organic compounds (VOCs) in industrial flue gases has emerged as a critical challenge for air pollution control[1,2]. These pollutants are not only toxic and carcinogenic themselves but also serve as key precursors to ozone (O_3) and particulate matter ($PM_{2.5}$)[3-6]. Catalytic oxidation for the removal of VOCs and selective catalytic reduction (SCR) for NO_x removal are widely recognized as the most effective end-of-pipe control technologies[7,8]. Consequently, the development of bifunctional catalysts capable of simultaneously and efficiently removing NO_x and VOCs has become a frontier topic in the field of multipollutant simultaneous control.

Transition metal oxide catalysts have demonstrated considerable potential for simultaneous removal applications[9]. Manganese-based spinel oxides, in particular, have attracted substantial attention due to their excellent redox properties and wide range of accessible oxidation states, exhibiting great promise in both low-temperature SCR and the catalytic oxidation of VOCs[10,11]. Spinel oxides with the general formula AB_2O_4 consist of tetrahedral [AO_4] and octahedral [BO_6] coordination units, whose unique crystal structure endows them with high tunability in both chemical composition and electronic structure[12,13]. The A and B sites can simultaneously accommodate multiple transition metal cations, providing a versatile platform for tailoring catalytic performance through elemental doping strategies[14,15]. Previous studies have reported improved catalytic VOCs oxidation and NO_x removal after the incorporation of two or more transition metals into spinel lattices, commonly attributing the improvement to synergistic interactions among the metals[16-18]. For instance, $CoMn_2O_4$, $NiMn_2O_4$, and $CuMn_2O_4$ spinels exhibited a pronounced A-site metal dependence in the synergistic catalytic degradation of benzene and toluene, with $CuMn_2O_4$ demonstrating far superior catalytic activity to $CoMn_2O_4$ and $NiMn_2O_4$[12]. Zhao *et al.* systematically investigated Mn-based spinels with different A-site metals (Cr, Fe, Co, Ni) for NH_3-SCR and chlorobenzene oxidation, and reported that $CrMn_2O_4$ exhibited the best performance in both reactions[11]. However, the microscopic mechanisms by which A-site metals influence catalytic performance remain insufficiently understood.

In recent years, superexchange interaction has attracted considerable attention as an emerging strategy for modulating the electronic structure of transition metal oxides[19,20]. Superexchange interaction refers to the indirect exchange coupling between two transition metal ions mediated through an oxygen bridge (M_1-O-M_2), which effectively regulates the valence states, spin states, and orbital occupations of metal ions[21,22]. In the field of battery materials, Zheng *et al.* have demonstrated that superexchange interaction can modulate the Ni/Mn spin states and trigger the Ni t_{2g}/O 2p reductive coupling mechanism, significantly enhancing the cycling stability of materials[23]. In the catalytic field, Wu *et al.* reported that the Fe^{3+}-O-Mn^{3+} superexchange interaction in $Fe_{2-x}Mn_xO_3$ perovskite induced a threefold increase in the reaction rate constant for hexabromocyclododecane (HBCD) catalytic oxidation, accompanied by a valence change from Fe^{3+} + Mn^{3+} to Fe^{2+} + Mn^{4+}[24]. More recently, Liu *et al.* identified two superexchange interactions in Mn-Cu spinels that depend on the geometric configuration of the metal sites[25]. The toluene-specific reaction rate increased fivefold in association with Mn_{oct}-O-Cu_{tet} interactions, whereas Mn_{oct}-O-Cu_{oct} interactions had an inhibitory effect. Although previous work primarily focused on the oxidation of individual VOCs, extending this superexchange strategy to the simultaneous

removal of NO_x and C_3H_8 is more complex, requiring a delicate balance between oxidation capability and effective NH_3 utilization. These findings indicate that superexchange interaction can fundamentally influence the redox properties of catalysts by modulating metal-oxygen bond strength, inducing surface electron redistribution, and activating oxygen species. Nevertheless, the interplay between A-O-Mn superexchange interactions and the orbital-level electronic structure of Mn-based spinels remains inadequately explored. Specifically, critical questions remain about how different A-site cations modulate the Mn d-band and O p-band centers, how this modulation affects orbital overlap and Mn–O bond covalency, and how these changes govern reaction pathways and catalytic performance in the simultaneous removal of NO_x and C_3H_8.

Herein, we successfully synthesized a series of AMn_2O_4 (A = Co, Ni, Cu, Zn) catalysts alongside a $CeMn_2O_x$ for the simultaneous removal of NO_x and C_3H_8. Experimental characterization and density functional theory (DFT) calculations were combined to systematically elucidate the mechanistic origins of A-O-Mn superexchange interactions and their orbital-level regulation of electron transfer and oxygen-species activation. This work aims to establish a robust structure-activity relationship that can guide the rational design of high-performance spinel catalysts for the simultaneous removal of NO_x and C_3H_8.

EXPERIMENTAL

Catalyst preparation

The AMn_2O_4 catalysts (A = Co, Ni, Cu, Zn) alongside a $CeMn_2O_x$ mixed-oxide reference sample were prepared by an oxalate precipitation method. 0.04 mol of $Mn(CH_3CO_2)_2$ and 0.02 mol of the acetate of metal A (A = Co, Ni, Cu, Zn, or Ce) were dissolved in a mixture of ethanol (75 mL) and deionized water (75 mL) by stirring at 500 rpm and 25 °C for 20 min until complete dissolution. Separately, oxalic acid (0.063 mol) was dissolved in ethanol (100 mL) by stirring at 500 rpm and 25 °C for 20 min until complete dissolution. The ethanolic oxalic acid solution was then rapidly introduced into the mixed metal acetate solution, followed by vigorous stirring for 0.5 h at 25 °C. After centrifugation, the collected precipitate was dried overnight under vacuum at 60 °C. The dried precipitates were subsequently calcined at 350 °C for 2 h using a heating rate of 5 °C·min^{-1} to obtain the AMn_2O_4 spinel catalysts.

Catalyst characterization

Scanning electron microscopy (SEM), transmission electron microscopy (TEM), energy-dispersive X-ray spectroscopy (EDS) mapping, electron paramagnetic resonance (EPR), Brunauer-Emmett-Teller (BET) analysis, O_2/NH_3 temperature-programmed desorption (TPD), H_2 temperature-programmed reduction (TPR), X-ray diffraction (XRD), Raman spectroscopy, DFT calculations, and *in situ* diffuse reflectance infrared Fourier transform spectroscopy (DRIFTS) were used to characterize the catalysts, as described in the Supplementary Materials.

Catalyst activity test

Activity measurements were performed at atmospheric pressure in a fixed-bed quartz reactor with an inner diameter of 6 mm; further details are provided in the Supplementary Materials.

Theoretical calculations

Spin-polarized DFT calculations were carried out in the Vienna *Ab initio* Simulation Package (VASP), using the Perdew-Burke-Ernzerhof (PBE) functional within the generalized gradient approximation (GGA)[26-28]. The projector augmented-wave (PAW) method was used to describe the ionic cores and valence electrons, with a plane-wave kinetic energy cutoff of 450 eV[29]. A Gaussian smearing width of 0.05 eV was applied to the partial occupancies of the Kohn-Sham orbitals. Self-consistency was reached when the change in electronic energy fell below 10^{-5} eV. Geometry optimization was considered converged when the force change was below 0.02 eV/Å. Dispersion interactions were described using Grimme's DFT-D3 method[30]. A 15 Å vacuum spacing was used perpendicular to the structural plane. For the surface structures, Brillouin-zone integration used a 1 × 1 × 1 Monkhorst-Pack k-point mesh.

To accurately describe the strongly correlated 3d electrons, the DFT+U method (Dudarev's approach, LDAUTYPE=2) was employed with LMAXMIX=4, and spin polarization (ISPIN=2) was enabled. The effective Hubbard *U* values ($U_{eff} = U - J$) and initial magnetic moments (MAGMOM) were set as fol-

lows: U_{eff} = 3.9-4.0 eV and an initial magnetic moment of 4.0 μB for Mn; U_{eff} = 6.0 eV and an initial magnetic moment of 1.0 μB for both Cu and Ni; and no U correction and an initial magnetic moment of 0.0 μB for Zn and O.

The oxygen chemical potential was calculated using a spin-polarized isolated O_2 molecule as the reference state. The O_2 molecule was placed in a 15 × 15 × 15 Å cubic supercell with Γ-point sampling. Spin polarization (ISPIN=2) was enabled to ensure convergence to a triplet state with a total magnetic moment of approximately 2 μB. Structural optimization used a 450 eV cutoff energy and a force convergence criterion of 0.02 eV/Å.

$^{18}O_2$ isotope experiment

In situ DRIFTS coupled with online mass spectrometry (MS) was used to track propane oxidation with $^{18}O_2$, as detailed in the Supplementary Materials.

RESULTS AND DISCUSSION

The structures and morphologies of AMn_2O_4

The XRD patterns in Figure 1A confirm that the synthesized catalysts possess spinel structures. All diffraction peaks of $CoMn_2O_4$ were well indexed to the tetragonal spinel structure[31,32] with reference to the Joint Committee on Powder Diffraction Standards (JCPDS) Powder Diffraction File (PDF)#00-055-0685, while $CuMn_2O_4$ and $NiMn_2O_4$ exhibited diffraction features characteristic of cubic spinel phases (JCPDS PDF#04-005-6874 and JCPDS PDF#00-001-1110, respectively)[25,33]. For $ZnMn_2O_4$, the reflections were readily assigned to a tetragonal spinel structure (JCPDS PDF#97-001-5305)[34]. For $CeMn_2O_x$, the diffraction pattern indicated the coexistence of cubic fluorite-type CeO_2 (PDF#97-002-8709) and tetragonal spinel Mn_3O_4 (PDF#04-002-3815)[35]. In addition to the XRD results, inductively coupled plasma (ICP) measurements [Supplementary Table 1] reveal that the elemental compositions of the catalysts closely match the nominal 1:2 A-to-Mn molar ratio, further confirming the formation of the spinel framework. SEM and TEM were used to examine the morphology and microstructure of the synthesized samples. As shown in Figure 1B and Supplementary Figure 1, all as-prepared samples consist of aggregated particles with irregular shapes. The EDS maps in Figure 1B showed a uniform distribution of the elements. TEM images in Figure 1B also confirmed the formation of the spinel phase. For $CoMn_2O_4$, lattice fringes with spacings of 0.247, 0.153, and 0.242 nm were indexed to the (311), (404), and (222) facets, respectively. The 0.210 and 0.240 nm lattice fringes were associated with the (400) and (222) planes of $NiMn_2O_4$, respectively. For $CuMn_2O_4$, the observed spacings of 0.249 and 0.481 nm corresponded to the (311) and (111) planes, respectively. Lattice fringes at 0.247, 0.484, and 0.300 nm were associated with the (211), (101), and (112) planes of $ZnMn_2O_4$, respectively. The lattice fringe spacings of 0.246, 0.308, and 0.310 nm were associated with the (202), (112), and (111) planes of Mn_3O_4 and CeO_2, respectively. These findings were consistent with the XRD data and confirmed the successful synthesis of the spinel catalysts. All AMn_2O_4 catalysts displayed type IV N_2 adsorption-desorption isotherms with characteristic H3 hysteresis loops [Figure 1D], indicating a predominance of mesopores[36,37]. $NiMn_2O_4$ had the largest BET surface area [Supplementary Table 2], which may provide more active sites for simultaneous C_3H_8 and NO_x removal.

We further investigated the structure of AMn_2O_4 catalysts using Raman spectroscopy [Figure 1F]. The Raman spectra of all as-prepared samples correspond to the typical vibration modes of the spinel structure. The Raman features at 173, 299, 347 and 496 cm^{-1} were assigned to the $F_{2g}^{(1)}$, T_{2g}, E_g and $F_{2g}^{(2)}$ modes[38]. The peak at 439 cm^{-1} was attributable to the F_{2g} mode of fluorite-structured CeO_2[16]. Notably, the A_{1g} characteristic peak was observed in the 620-650 cm^{-1} range for the Mn-based spinel catalysts with various A-site metal dopants (Co, Ni, Cu, Zn, Ce). The A_{1g} modes arise from symmetric Mn–O stretching within MnO_6 octahedra ($[MnO_6]_{oct}$), a characteristic vibration of the spinel structure[36]. The doping of different A-site metals induced a red shift in the Mn–O symmetric stretching peak. The red shift indicated a weakening of the Mn–O bond that facilitated its cleavage and thereby promoted the formation and migration of oxygen species, ultimately enhancing the catalytic activity[37]. Among the samples, $NiMn_2O_4$ exhibited the lowest A_{1g} peak wavenumber (621 cm^{-1}), which was consistent with its superior catalytic performance in the activity tests.

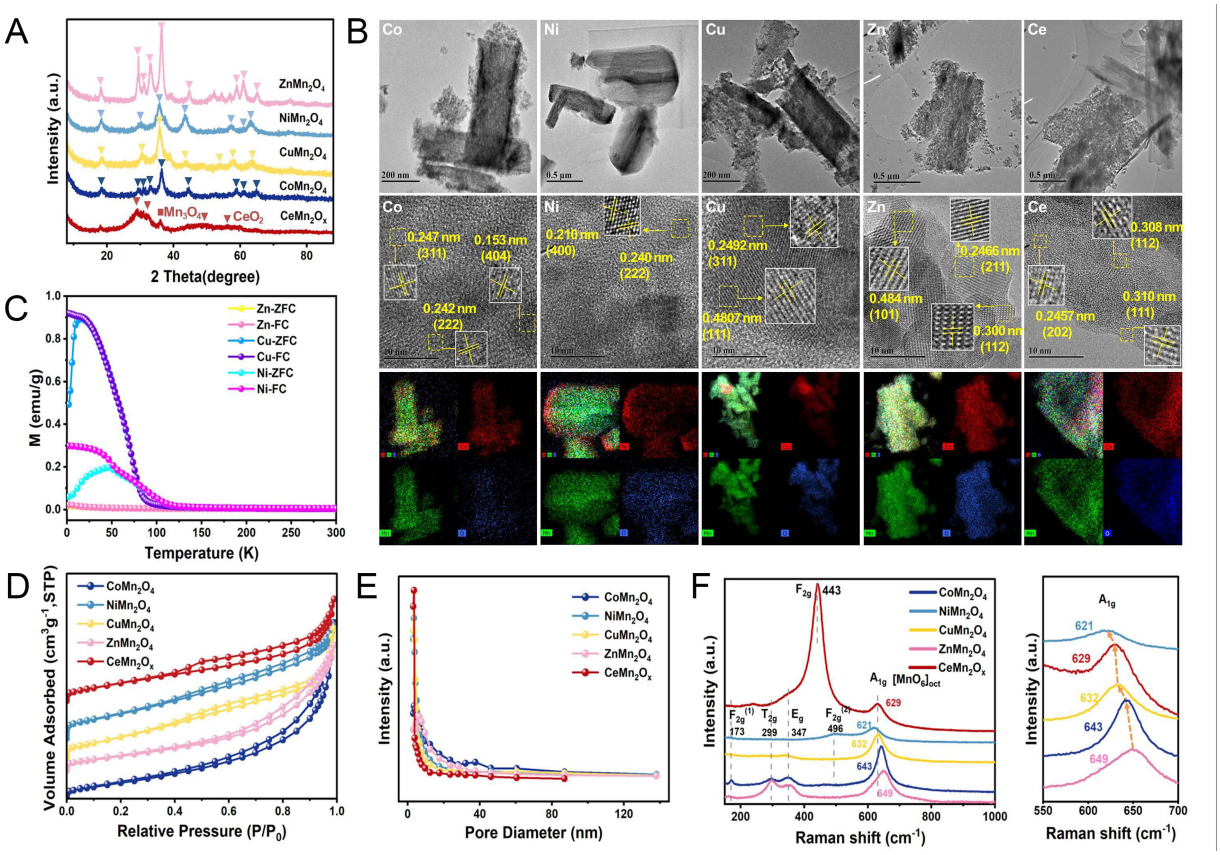


Figure 1. (A) XRD patterns; (B) TEM and elemental mapping images; (C) ZFC and FC magnetization curves for AMn_2O_4 samples (A = Ni, Cu, or Zn); (D) N_2 adsorption-desorption isotherms; (E) pore-size distribution; and (F) Raman spectra of AMn_2O_4. ZFC: Zero-field-cooled; FC: field-cooled.

Catalytic performance

The simultaneous removal performance of NO_x and C_3H_8 over the AMn_2O_4 catalysts is shown in Figure 2, with the corresponding activity evaluation data summarized in Supplementary Table 3. In the absence of SO_2, the catalytic activity of the prepared catalysts varied significantly with the A-site metal. Notably, the $NiMn_2O_4$ catalyst exhibited the best overall performance, achieving 91.42% C_3H_8 conversion and 92.83% NO_x conversion simultaneously at 220 °C, along with the highest N_2 selectivity. Although $CoMn_2O_4$ showed the lowest T_{90} (the temperature required to achieve 90% C_3H_8 conversion) for C_3H_8 oxidation, its N_2 selectivity was inferior. This is attributed to the excessively strong oxidizing properties of $CoMn_2O_4$, which promoted the over-oxidation of NH_3. Therefore, the moderate redox properties of $NiMn_2O_4$ are more favorable for the simultaneous reaction. Furthermore, the CO_2 selectivity approached 100% for all samples, particularly at higher temperatures (200-300 °C) [Figure 2B], suggesting satisfactory deep mineralization of C_3H_8 over the synthesized AMn_2O_4 catalysts. The apparent activation energies (E_a) obtained from the Arrhenius equation provided further support for these findings. The relatively low activation energies of $NiMn_2O_4$ explain its high catalytic performance in the simultaneous removal of both pollutants, which is consistent with the findings from the activity tests. The impact of 40 ppm SO_2 on the catalyst's performance was shown in Supplementary Figure 2. At 220 °C, the NO_x conversion over $NiMn_2O_4$ reached 93.84%, while the C_3H_8 conversion decreased to 80.79%. Compared with the SO_2-free condition, the T_{90} for C_3H_8 increased by 6 °C, and the CO_2 selectivity slightly declined. However, the denitrification activity window significantly broadened [the temperature required to achieve 90% NO_x conversion (T_{90}): 150-300 °C *vs.* 150-222 °C], indicating enhanced denitrification activity. Moreover, the N_2 selectivity was notably improved under sulfur-containing conditions, which could be attributed to

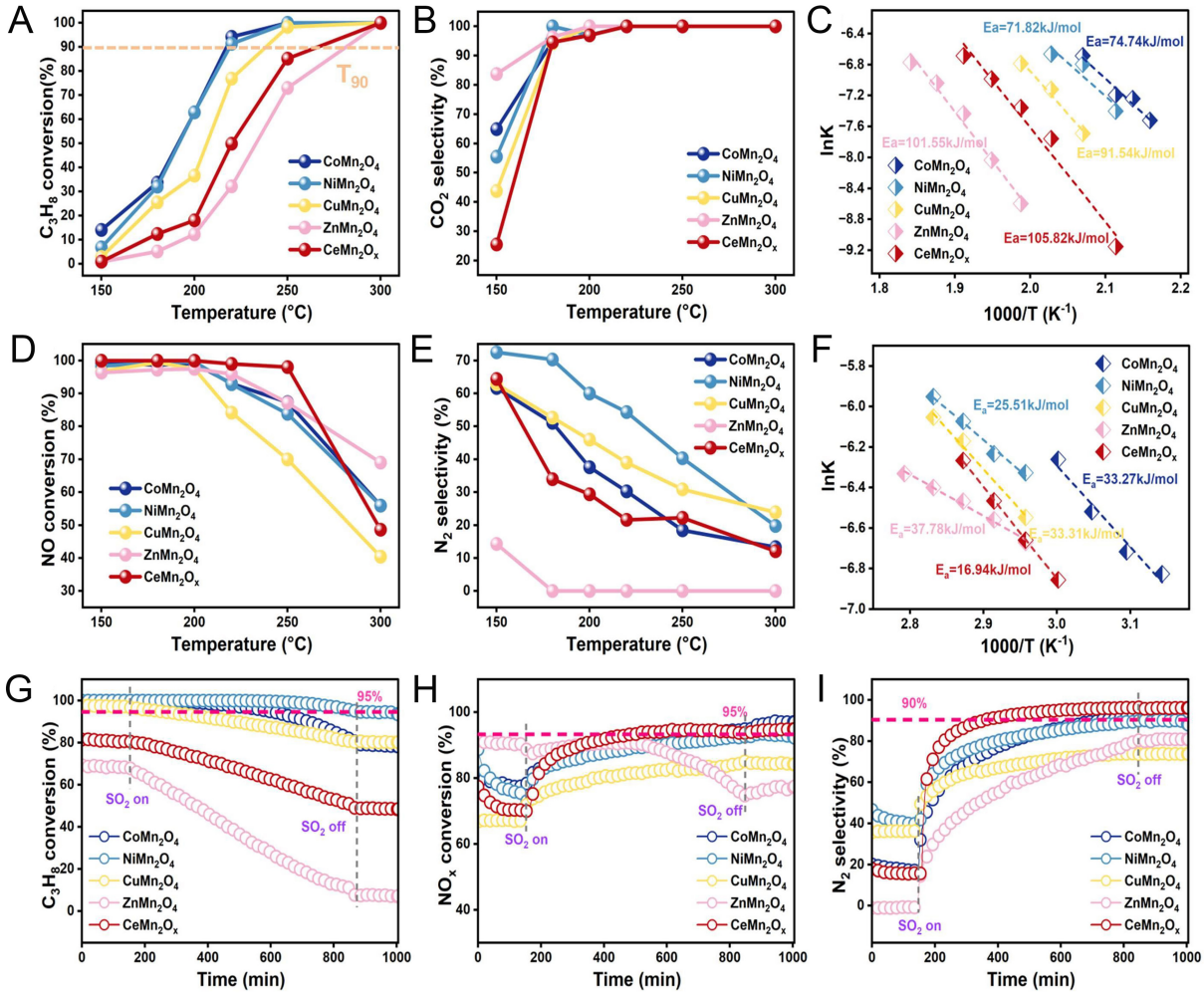


Figure 2. (A and D) C_3H_8 and NO conversions; (B and E) CO_2 and N_2 selectivities; (C and F) Arrhenius plots of C_3H_8 oxidation and NH_3-SCR; and (G-I) stability tests on AMn_2O_4. Reaction conditions: 500 ppm NH_3, 500 ppm NO, 500 ppm C_3H_8, 40 ppm SO_2 (when used), 5 vol% O_2, N_2 as the balance gas, 30,000 mL g^{-1} h^{-1}. Stability-test temperature: 250 °C. SCR: Selective catalytic reduction.

the combination of SO_2 with NH_3 that suppressed the over-oxidation of NH_3 and reduced the formation of the by-product N_2O, thus enhancing N_2 selectivity. Stability tests conducted in the presence of SO_2 revealed that after SO_2 was cut off, the conversions of NO_x and C_3H_8 both remained above 95%, and the N_2 selectivity exceeded 90%. Collectively, these findings demonstrate the superior SO_2 tolerance of the $NiMn_2O_4$ catalyst. SO_2 exerts a pronounced negative effect on the oxidation activity and selectivity of C_3H_8 at low temperatures, while considerably boosting the NH_3-SCR performance.

Furthermore, the water resistance of $NiMn_2O_4$ was evaluated under simultaneous-removal conditions. Upon introducing water vapor at 3 vol%, the NO conversion increased from 87.4% to 95.2%, whereas the C_3H_8 conversion decreased from 97.9% to 87.7% [Supplementary Figure 3]. One possible explanation for the increased NO conversion is that H_2O dissociation formed surface hydroxyl groups, providing additional Brønsted acid sites that could facilitate NH_3 adsorption and activation. Water adsorption may also have partially occupied strongly oxidizing sites, thereby suppressing the non-selective over-oxidation of NH_3. In contrast, competitive adsorption of H_2O and C_3H_8 on the active sites may have contributed to the temporary decrease in C_3H_8 conversion[39]. After the water feed was discontinued, both conversions recovered to their initial levels, indicating that the effects of water were reversible under the tested conditions. Furthermore, transient experiments were performed to investigate the interplay between

propane and NO_x. The detailed data and discussion in Supplementary Figure 4 demonstrate that $NiMn_2O_4$ can accommodate propane oxidation and NH_3-SCR simultaneously with limited performance penalties under the tested conditions.

Superexchange-modulated electronic structure and surface acidity

To investigate the reasons for the optimal activity of $NiMn_2O_4$, we examined the surface chemical states via X-ray photoelectron spectroscopy (XPS) [Figure 3] and further verified the spin-mediated magnetic exchange coupling and local coordination environment via X-ray absorption fine structure (XAFS) [Supplementary Figure 5] and zero-field--cooled/field-cooled (ZFC/FC) measurements [Figure 1C and Supplementary Figure 6], as detailed in the Supplementary Materials. The Curie-Weiss fitting was performed on the FC magnetic susceptibility data (200-280 K) to evaluate the magnetic interactions, with the calculated θ, μ_{eff}, and R^2 values presented in Supplementary Tables 4 and 5. The Mn $2p_{3/2}$ spectra were deconvoluted using a multiplet-splitting fitting approach with physically constrained binding energies and relative intensities. Independent Mn 3s XPS [Supplementary Figure 7] and Mn K-edge X-ray absorption near-edge structure (XANES) measurements further validated the valence states. The binding energy shifts observed upon elemental doping further indicate the electronic interaction between Mn and the dopants[40,41]. The Mn^{4+}/Mn ratio [Supplementary Table 6] followed the order of $NiMn_2O_4$ > $CoMn_2O_4$ > $CuMn_2O_4$ > $CeMn_2O_x$ > $ZnMn_2O_4$, indicating that the Ni-O-Mn superexchange interaction most effectively stabilized Mn^{4+}. In the spinel crystal, strong electronic interactions between octahedral Mn^{3+} and Ni^{3+} induce electron rearrangement via superexchange mediated by bridging oxygen atoms, consistent with the reaction $Mn^{3+} + Ni^{3+} \rightarrow Mn^{4+} + Ni^{2+}$. Along the octahedral-O-octahedral backbone of the spinel, this superexchange facilitates indirect electron migration from the degenerate e_g orbitals of Mn^{3+} to the e_g orbitals of Ni^{3+}, consequently raising and maintaining the surface Mn^{4+} concentration [Figure 4]. Based on the electron localization function (ELF) and charge density difference (CDD) analyses, the superior superexchange interactions of $NiMn_2O_4$ can be rationalized. The ELF analysis revealed that $NiMn_2O_4$ exhibited the most diffuse electron distribution along the Mn–O direction, as reflected by the lowest ELF values in the Mn–O bonding region [Figure 3G]. This indicated that the bridging oxygen electrons underwent the highest degree of delocalization, which originated from the electronic connectivity established by the Ni-O-Mn superexchange network. This high degree of delocalization reduced structural relaxation and lowered the energy barrier for lattice oxygen activation. (Further discussion regarding the modulation of oxygen species activation via Ni-O-Mn superexchange interactions is provided in Section "Superexchange-modulated oxygen species activation".) The CDD analysis further corroborated this interpretation [Figure 3H]. In $NiMn_2O_4$, pronounced charge depletion was observed at both Ni_{oct} and Mn_{oct} sites, with both extending toward the bridging oxygen, thereby forming a contiguous Ni_{oct}-O-Mn_{oct} charge-transfer channel. This three-center charge connectivity provided direct electronic evidence for the Ni-O-Mn superexchange interaction. Moreover, $NiMn_2O_4$ exhibited the strongest charge depletion at the Mn_{oct} site. In contrast, $CuMn_2O_4$ and $ZnMn_2O_4$ exhibited charge transfer largely confined to local Mn_{oct}–O bonds with weaker charge depletion than $NiMn_2O_4$. Consequently, the Ni-O-Mn superexchange interaction in $NiMn_2O_4$ establishes an efficient electron transfer channel that stabilizes the surface Mn^{4+} species and increases their proportion, thereby providing the strongest acid sites, which are predominantly Lewis acid sites and promote the adsorption and activation of NH_3 and C_3H_8[42].

The acid sites of the catalysts were characterized by NH_3-TPD [Figure 3D and E]. The NH_3 desorption profiles were divided into three temperature regions corresponding to weak (< 200 °C), medium (200-400 °C), and strong (> 400 °C) acid sites[43]. Among all the samples, $NiMn_2O_4$ exhibited the highest total acidity [Figure 3E and Supplementary Table 7], which promoted the adsorption and conversion of both C_3H_8 and NH_3. To account for differences in specific surface area, we have additionally normalized the NH_3-TPD-derived uptake by the BET surface area according to $q_{area} = q_{mass}/S_{BET}$. The corrected results are presented in Supplementary Table 8. $NiMn_2O_4$ exhibits the highest measured total NH_3 uptake on both a mass basis (212.2 μmol·g^{-1}) and a BET surface-area basis (1.1 μmol·m^{-2}). Thus, its high-

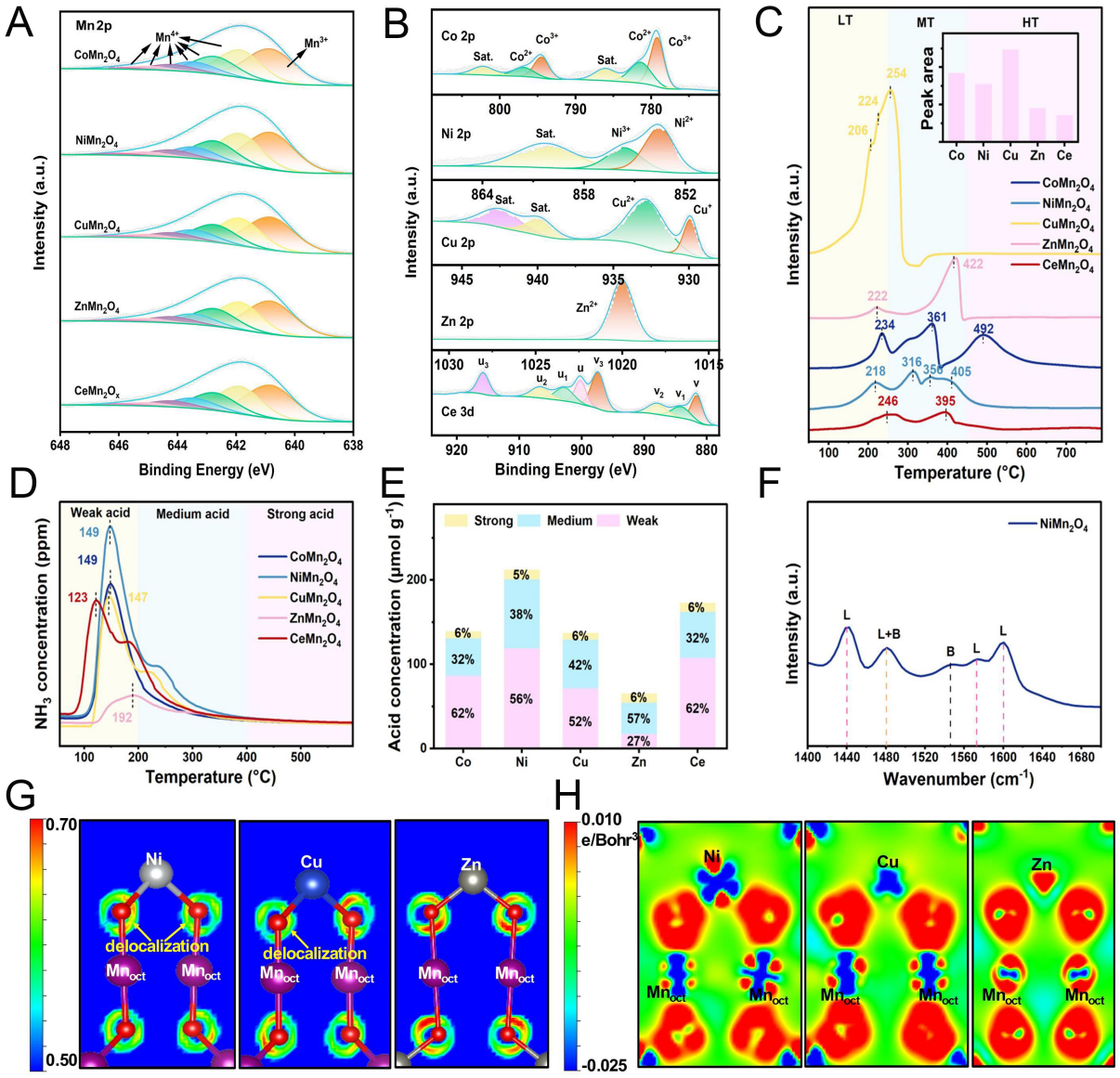


Figure 3. XPS spectra of (A) Mn 2p and (B) A-site metal 2p (A = Co, Ni, Cu, or Zn) and Ce 3d for the investigated catalysts; (C) H_2-TPR profiles of AMn_2O_4; (D and E) NH_3-TPD profiles; (F) Py-IR spectra of $NiMn_2O_4$; (G) ELF plots; and (H) charge-density-difference maps (charge accumulation and depletion are shown in red and blue, respectively). XPS: X-ray photoelectron spectroscopy; TPR: temperature-programmed reduction; TPD: temperature-programmed desorption; Py-IR: pyridine-adsorption Fourier-transform infrared; ELF: electron localization function; LT: low temperature; MT: medium temperature; HT: high temperature.

er mass-based uptake cannot be attributed solely to its larger BET surface area. To identify the acid-site types, we also conducted pyridine-adsorption Fourier-transform infrared (Py-IR) measurements [Figure 3F]. The analysis indicates that approximately 88% of the quantified acid sites on $NiMn_2O_4$ are Lewis acid sites [Supplementary Table 9].

H_2-TPR was further used to assess the redox properties of the AMn_2O_4 spinel oxides [Figure 3]. Three distinct reduction peaks were observed for $CoMn_2O_4$ at 234, 361, and 492 °C. The peak at the lowest temperature was attributed to overlapping reductions of $Mn^{4+} \rightarrow Mn^{3+}$ and $Co^{3+} \rightarrow Co^{2+}$, while the peaks at 361 and 492 °C were assigned to $Mn^{3+} \rightarrow Mn^{2+}$ and $Co^{2+} \rightarrow Co^0$ reductions, respectively[44]. For $NiMn_2O_4$, reduction peaks were observed at 218, 316, 356, and 405 °C and were attributed to $Mn^{4+} \rightarrow Mn^{3+}$, $Mn^{3+} \rightarrow Mn^{2+}$, and $Ni^{2+} \rightarrow Ni^0$ reduction processes, respectively[45]. $CuMn_2O_4$ showed reduction peaks at 206, 224, and 254 °C, substantially lower than those of other samples. The low-temperature

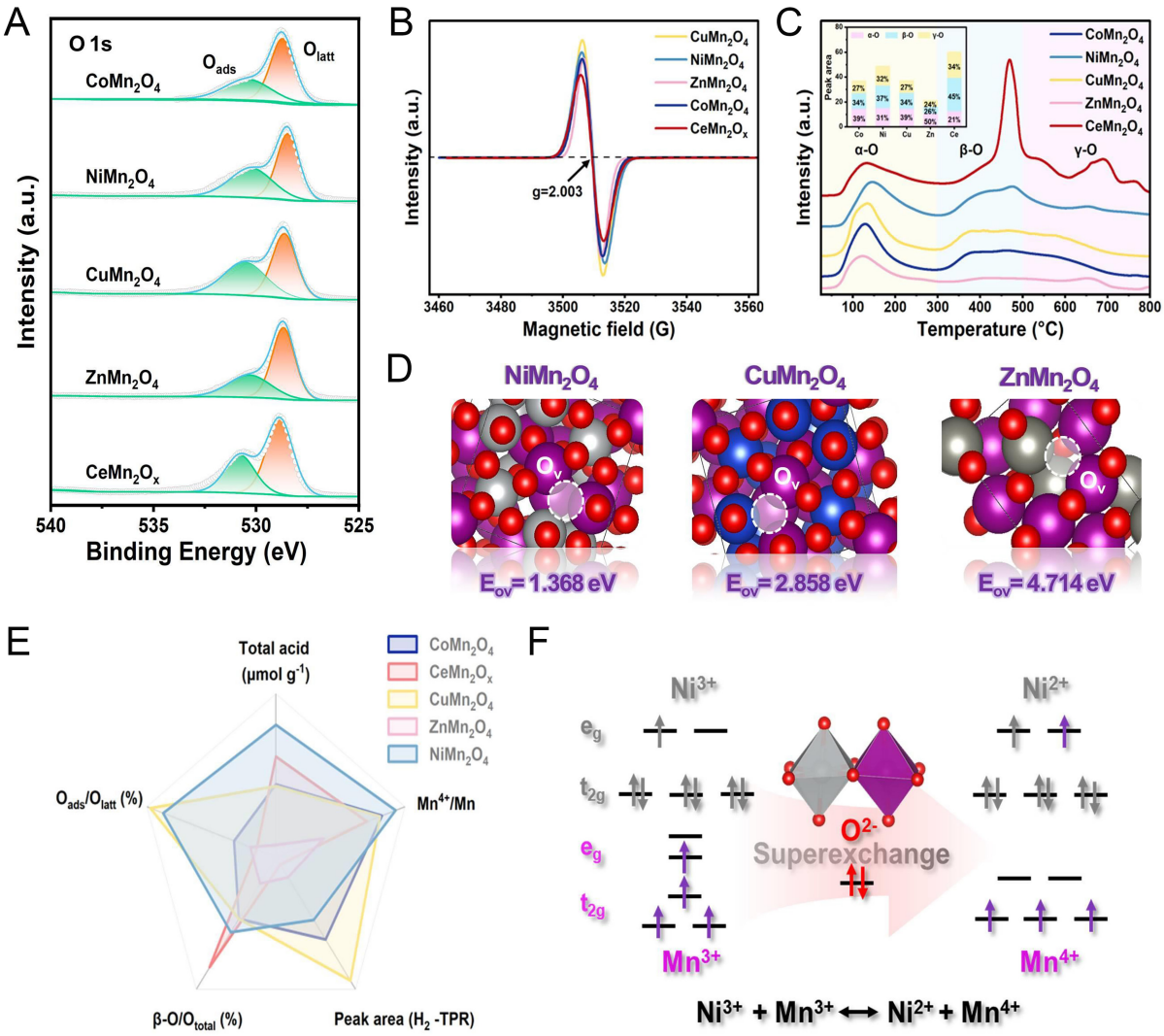


Figure 4. (A) O 1s XPS spectra, (B) EPR spectra, and (C) O_2-TPD profiles of AMn_2O_4; (D) oxygen-vacancy formation energies of AMn_2O_4; (E) radar plot comparing catalyst performance; and (F) schematic illustration of the Ni-O-Mn superexchange interaction. XPS: X-ray photoelectron spectroscopy; EPR: electron paramagnetic resonance; TPD: temperature-programmed desorption.

peaks (206 and 224 °C) were attributed to the overlapping of $Cu^{2+} \rightarrow Cu^0$ and $Mn^{4+} \rightarrow Mn^{3+}$ reduction, that the peak at 254 °C corresponds to $Mn^{3+} \rightarrow Mn^{2+}$[46]. This reduction consumed substantial hydrogen and converted Cu^{2+} to metallic Cu^0 at low temperatures. This deep reduction disrupted the Cu-O-Mn bridging connectivity and consequently suppressed the synergistic Cu^+/Cu^{2+} and Mn^{4+}/Mn^{3+} redox cycle, ultimately leading to inferior catalytic performance despite the high apparent reducibility. In contrast, although $NiMn_2O_4$ showed higher reduction temperatures than $CuMn_2O_4$, its reduction peaks corresponded predominantly to the reversible Mn^{4+}/Mn^{3+} redox cycle rather than irreversible deep reduction, indicating efficient and sustainable cycling of Mn oxidation states. The peaks of $ZnMn_2O_4$ at 222 and 422 °C were attributed to the stepwise reduction of Mn species from Mn^{4+} to Mn^{3+} and then to Mn^{2+}. The reduction peaks of $CeMn_2O_x$ at 246 and 395 °C were assigned to $Mn^{4+} \rightarrow Mn^{3+}$ reduction and the coupled reduction of $Mn^{3+} \rightarrow Mn^{2+}$ and $Ce^{4+} \rightarrow Ce^{3+}$, respectively[47].

Superexchange-modulated oxygen species activation

In the Mars-van Krevelen (MvK) cycle, C_3H_8 oxidation involves consumption of lattice oxygen, formation of vacancies, and replenishment by gaseous O_2. In this section, we discuss how superexchange interactions modulate the activation of oxygen species

and consequently influence catalytic activity.

The oxygen vacancy formation energy (E_{vac}) was quantitatively evaluated by DFT calculations. As shown in Figure 4 and Supplementary Table 10, the E_{vac} values followed the order of $ZnMn_2O_4$ (4.714 eV) > $CuMn_2O_4$ (2.858 eV) > $NiMn_2O_4$ (1.368 eV). The substantially lower E_{vac} of $NiMn_2O_4$ indicated that its lattice oxygen was the easiest to extract thermodynamically. This extraction step is the first and most energy-demanding of the MvK cycle, and therefore it is most readily initiated on $NiMn_2O_4$. This low E_{vac} arose from the electronic delocalization enabled by the Ni-O-Mn superexchange network. In contrast, $ZnMn_2O_4$ lacked any effective superexchange pathway due to the d^{10} electronic configuration of Zn^{2+}. The electronic network remained highly localized, affording no channel to disperse the excess charge following oxygen departure. Consequently, it suffered from the highest E_{vac} and the most constrained lattice oxygen mobility, consistent with its inferior catalytic performance.

The O 1s XPS spectra [Figure 4A] at 528.56-529.59 and 530.23-531.52 eV were assigned to surface lattice oxygen (O_{latt}) and adsorbed oxygen species (O_{ads}), respectively[48]. As shown in Supplementary Table 6, $CuMn_2O_4$ exhibited the highest O_{ads}/O_{latt} ratio, while $NiMn_2O_4$ showed a slightly lower value. Consistent with this observation, the EPR results [Figure 4B] indicated that oxygen-vacancy concentrations followed the order $CuMn_2O_4$ > $NiMn_2O_4$ > $CoMn_2O_4$ > $ZnMn_2O_4$ > $CeMn_2O_x$. However, the oxygen vacancy concentration alone was insufficient to explain the catalytic activity trend. Notably, although $CuMn_2O_4$ possessed the highest O_{ads}/O_{latt} ratio and the strongest EPR signal, its actual catalytic performance was inferior to that of $NiMn_2O_4$, because its vacancies originated from Jahn-Teller distortion and served primarily to relieve lattice strain. $CuMn_2O_4$ exhibited a considerably higher E_{vac} than $NiMn_2O_4$. Upon oxygen removal, the excess electrons became trapped at adjacent metal sites due to the absence of a delocalization pathway, incurring a substantial structural relaxation energy. Once vacancies are formed, their replenishment relies on oxygen mobility, as evaluated by O_2-TPD.

O_2-TPD was used to evaluate oxygen mobility in the AMn_2O_4 samples [Figure 4C]. The desorption features in the ranges of 50-300, 300-500, and above 500 °C were assigned to surface-adsorbed oxygen species (α-O), surface lattice oxygen species (β-O), and bulk lattice oxygen species (γ-O), respectively[49,50]. Remarkably, the β-O/O_{total} ratio, which represents the most readily mobilizable oxygen species for the MvK mechanism, followed the order of $CeMn_2O_x$ > $NiMn_2O_4$ > $CoMn_2O_4$ ≈ $CuMn_2O_4$ > $ZnMn_2O_4$. Although $CeMn_2O_x$ possessed the strongest oxygen storage and release capacity, it exhibited the lowest oxygen-vacancy concentration and Mn^{4+} proportion, thus lacking efficient adsorption and activation sites for reactants. Although $CuMn_2O_4$ had the highest oxygen-vacancy concentration, these vacancies primarily stabilized the lattice rather than participating effectively in the catalytic cycle. The abundance of oxygen vacancies did not translate into effective oxygen release and migration. In contrast, the Ni-O-Mn superexchange interaction moderately weakened the Mn–O bond strength in $NiMn_2O_4$, resulting in both moderate oxygen mobility and a suitable oxygen vacancy concentration, thereby enabling lattice oxygen to efficiently participate in the reaction through a consumption-replenishment cycle (i.e., the MvK mechanism).

In summary, the Ni-O-Mn superexchange interaction exerts multifaceted control over oxygen species in $NiMn_2O_4$. It maintains an optimal vacancy concentration, minimizes the energy penalty for lattice oxygen extraction, and promotes the mobility of O_{latt}. This integrated regulation ensures the most favorable oxygen dynamics for the MvK cycle, ultimately conferring superior catalytic activity upon $NiMn_2O_4$. The radar chart [Figure 4E] summarizes the preceding sections and shows that $NiMn_2O_4$ exhibited balanced performance across all evaluated dimensions, with particularly high values for Mn^{4+} concentration, surface acidity, and oxygen mobility, which are key descriptors governing catalytic efficiency.

Orbital origin of Ni-O-Mn superexchange interaction

To gain deeper insight into the intrinsic mechanism behind the Ni-O-Mn superexchange effect, DFT simulations were performed to obtain surface-projected density of states (PDOS) of O 2p and Mn/A (Ni, Cu, Zn) 3d for $NiMn_2O_4$, $CuMn_2O_4$, and $ZnMn_2O_4$ [Figure 5A-C], together with schematic sketches of the

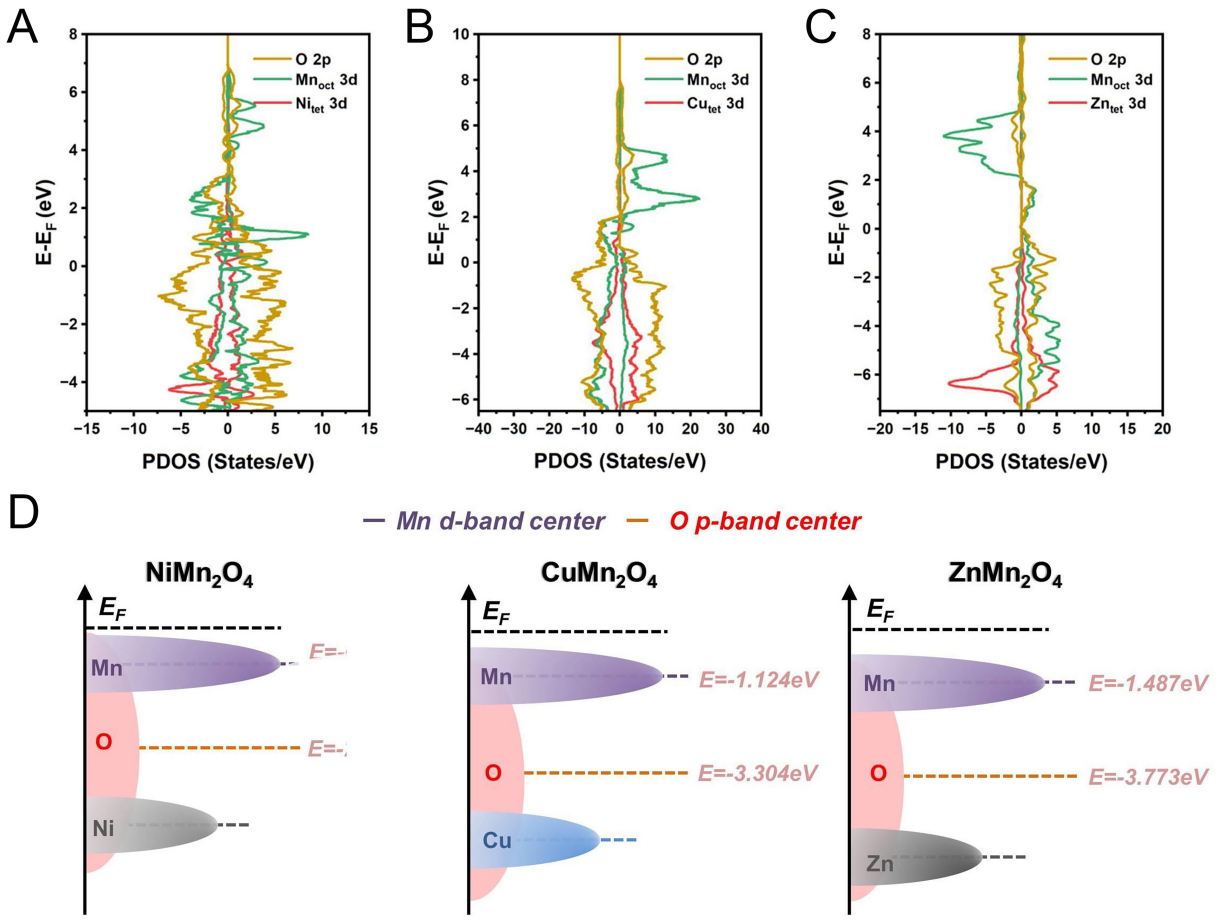


Figure 5. (A-C) Surface PDOS of O 2p and Mn/A (Ni, Cu, Zn); (D) Schematic of AMn_2O_4 electronic structures with Mn 3d-band and O 2p band centers. PDOS: Projected density of states.

relevant band centers. In $NiMn_2O_4$, the Mn 3d and O 2p orbitals exhibited pronounced overlap in the energy region immediately below the Fermi level, while the Ni 3d orbitals also contributed to this energy window, establishing a continuous Ni-O-Mn orbital connectivity that enabled three-center electron transfer from Mn to Ni through the bridging oxygen. In $CuMn_2O_4$, the Cu 3d states likewise fell within this energy window, yet the Mn–O overlap was comparatively weaker than in $NiMn_2O_4$. In $ZnMn_2O_4$, by contrast, the Zn 3d states were located deep below E_F owing to the fully filled d^{10} configuration of Zn^{2+}, so that no effective orbital channel participated in the near-E_F window and the superexchange pathway was essentially absent. Ni substitution induced strong Ni_{oct}-O-Mn_{oct} superexchange electronic interactions and shifted the Mn_{oct} d-band center upward relative to the Fermi level [Figure 5D]. Specifically, the Mn d-band center in $NiMn_2O_4$ was calculated to be -0.785 eV relative to the Fermi level, substantially higher than the values for $CuMn_2O_4$ (-1.124 eV) and $ZnMn_2O_4$ (-1.487 eV) [Supplementary Table 10]. An upshifted d-band center brought the Mn 3d states closer to the Fermi level and increased the filling of the Mn 3d-O 2p antibonding states, thereby weakening the Mn_{oct}–O bond[51]. Integrated crystal orbital Hamilton population (ICOHP) analysis provided further support for this electronic modulation [Supplementary Figure 8]. The -ICOHP values followed the order $NiMn_2O_4$ < $CuMn_2O_4$ < $ZnMn_2O_4$, confirming that the covalent bonding of Mn_{oct}–O was the weakest in $NiMn_2O_4$. The weakest Mn_{oct}–O bond directly rationalized the lowest E_{vac} of $NiMn_2O_4$ and the most facile lattice oxygen extraction. In addition, the Ni-O-Mn superexchange network enabled extensive electronic delocalization upon oxygen removal, as evidenced by the ELF [Figure 3G] and CDD [Figure 3H] analyses, which further dispersed excess electrons and reduced the structural relaxation energy, addition-

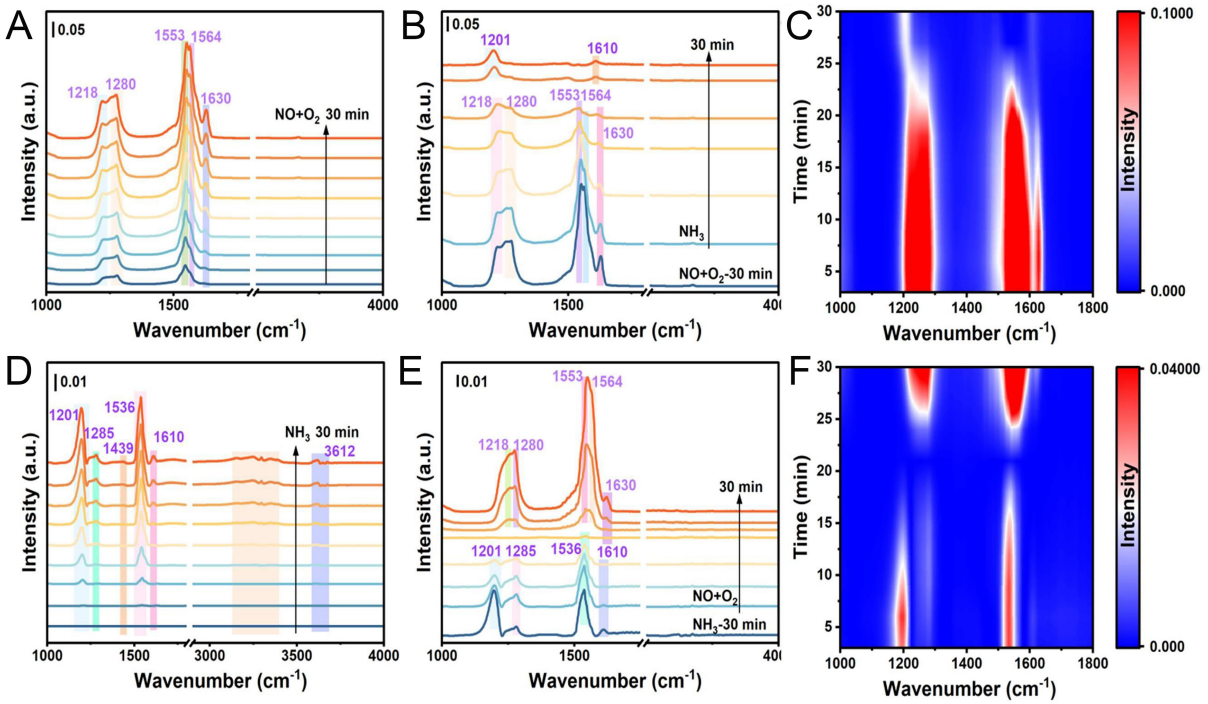


Figure 6. *In situ* DRIFTS spectra recorded at 230 °C during co-adsorption of 500 ppm NO + O_2 (A) and adsorption of 500 ppm NH_3 (D) over the $NiMn_2O_4$ catalyst; *in situ* DRIFTS spectra and corresponding 2D contour maps showing NH_3 reacting with pre-adsorbed NO + O_2 (B and C) and NO + O_2 reacting with pre-adsorbed NH_3 (E and F) over the $NiMn_2O_4$ catalyst. DRIFTS: Diffuse reflectance infrared Fourier transform spectroscopy.

ally stabilizing the oxygen-vacancy state. Consequently, the weakened Mn_{oct}–O bonds in $NiMn_2O_4$ facilitated oxygen extraction and replenishment during the catalytic cycle, consistent with the superior lattice-oxygen-involving MvK activity of $NiMn_2O_4$.

Reaction mechanism

Mechanism of NH_3-SCR

The evolution of surface species during NH_3-SCR over $NiMn_2O_4$ was investigated by *in situ* DRIFTS, using sequential reactions of NO + O_2 with pre-adsorbed NH_3 and of NH_3 with pre-adsorbed NO + O_2. In the *in situ* DRIFTS spectra of NO + O_2 adsorption [Figure 6A], several vibrational bands were observed at 1,218, 1,280, 1,553, 1,564, and 1,630 cm^{-1} as the adsorption time progressed. The bands at 1,218 and 1,630 cm^{-1} were assigned to the symmetric and asymmetric vibrations of bridging nitrate species, respectively[2]. The 1,280 cm^{-1} band was assigned to symmetric stretching of monodentate nitrate, whereas the 1,553 and 1,564 cm^{-1} bands were attributed to bidentate nitrate species[52]. The presence of these bands indicated that NO was oxidized on the catalyst surface, forming various nitrate adsorption species. The NO-derived bands became progressively stronger as the adsorption time increased. After NO + O_2 adsorption reached saturation, the gas stream was switched to NH_3 [Figure 6B and C]. The nitrate bands gradually diminished and eventually disappeared, accompanied by a concurrent enhancement of NH_3-related adsorption bands. These changes suggested a reaction between NH_3 and pre-adsorbed nitrate species, consistent with the Langmuir-Hinshelwood (L-H) mechanism.

Conversely, when the gas introduction order was reversed, NH_3 was first introduced onto the catalyst [Figure 6D]. The bands at 1,201, 1,285, and 1,610 cm^{-1} corresponded to bending vibrations of NH_3 coordinated to Lewis acid sites[53], whereas the 1,439 cm^{-1} band was assigned to bending of NH^{4+} species on Brønsted acid sites[54]. The broad feature at 3,100-3,400 cm^{-1} was assigned to N-H stretching vibrations of coordinated NH_3. The 1,536 cm^{-1} band was assigned to amide (-NH_2) species[55], indicating

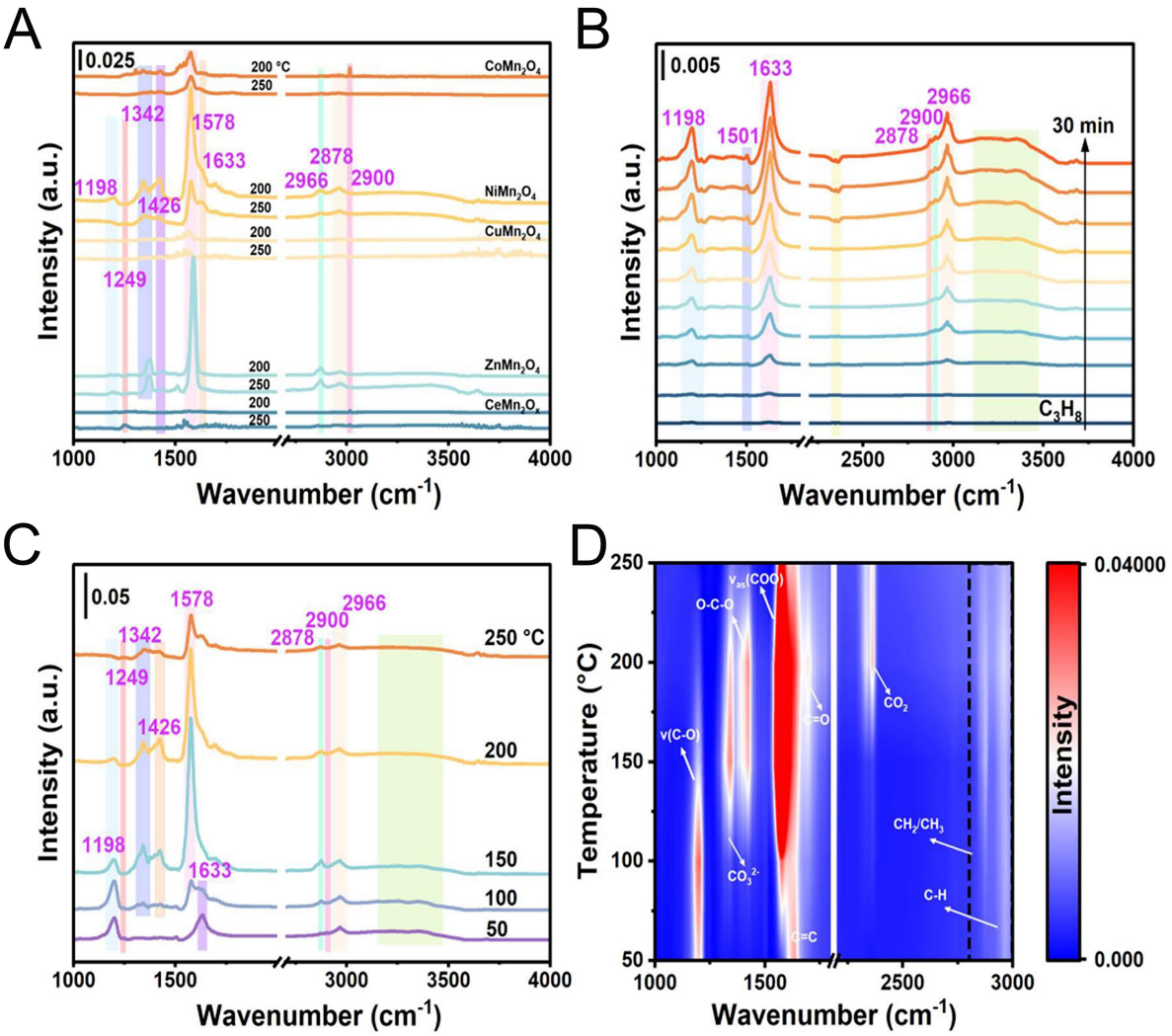


Figure 7. *In situ* DRIFTS spectra comparing C_3H_8 oxidation over AMn_2O_4 catalysts at 200 and 250 °C (A), C_3H_8 adsorption over $NiMn_2O_4$ at 50 °C (B), and C_3H_8 oxidation over $NiMn_2O_4$ from 50 to 250 °C (C), with the corresponding intensity plot shown in (D). DRIFTS: Diffuse reflectance infrared Fourier transform spectroscopy.

that a portion of the adsorbed NH_3 underwent dehydrogenation to form -NH_2 intermediates on the catalyst surface. The feature at 3,612 cm^{-1} was attributed to O-H stretching of isolated surface hydroxyl groups, suggesting that some hydroxyl species did not participate in adsorption. After NH_3 adsorption reached saturation, the gas stream was switched to NO + O_2 [Figure 6E and F]. The characteristic bands of NH_3 gradually weakened and vanished, while new nitrate bands at 1,218, 1,280, 1,553, 1,564, and 1,630 cm^{-1} emerged with a time-dependent increase in intensity. This result indicated that the Eley-Rideal (E-R) mechanism also operated through reaction between gaseous NO and surface-adsorbed NH_3 species. *In situ* DRIFTS coupled with online MS was employed to monitor the transient gas-phase products, thereby ruling out the possibilities of simple desorption or non-reactive site competition [Supplementary Figure 9]. A comparative study of NH_3-SCR over different spinel catalysts was conducted. As shown in Supplementary Figure 10, the NH_3-SCR reaction over all catalysts operated via concurrent L-H and E-R pathways. Notably, the Ni-O-Mn superexchange interaction modulated the Mn-site redox potential, conferring a moderate oxidative environment that neither facilitated over-oxidation of NH_3 to N_2O nor resulted in insufficient surface activation.

Mechanism of C_3H_8 oxidation

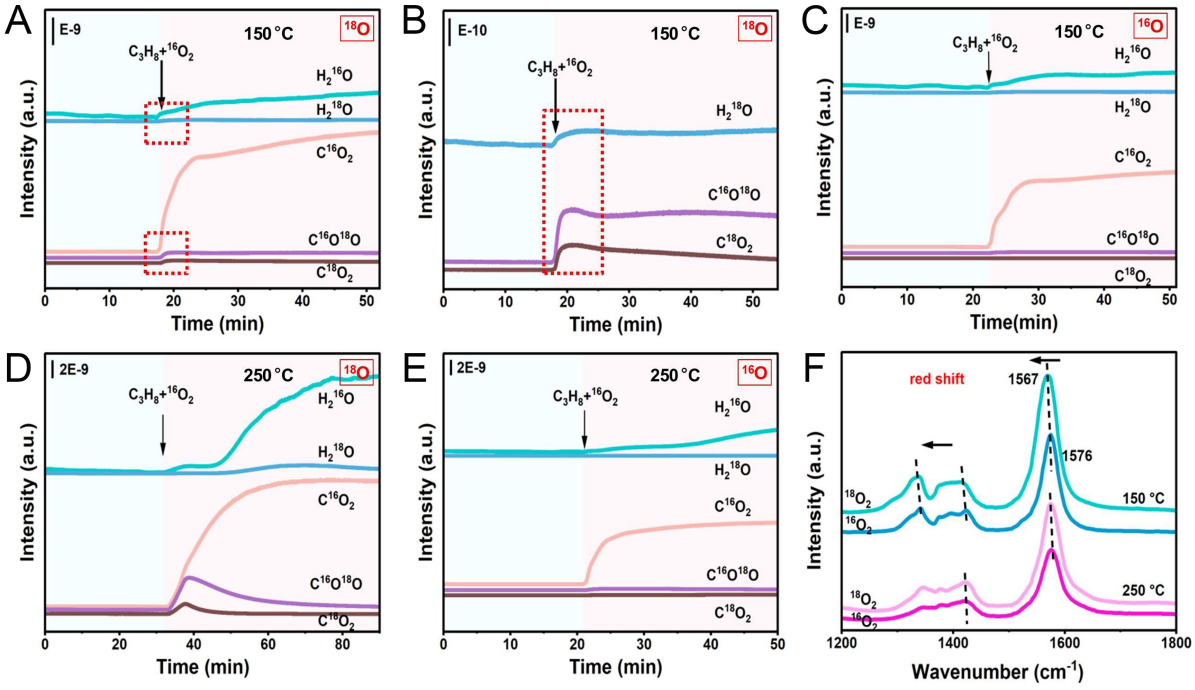


Figure 8. Time-dependent MS signals of the outlet gas at 150 °C over $NiMn_2O_4$ pretreated with $^{18}O_2$ (A and B) and $^{16}O_2$ (C); (D and E) Time-dependent MS signals of the outlet gas at 250 °C over $NiMn_2O_4$ pretreated with $^{18}O_2$ (D) and $^{16}O_2$ (E); (F) *In situ* DRIFTS spectra of surface species at 150 and 250 °C showing the red shift of characteristic bands. MS: Mass spectrometry; DRIFTS: diffuse reflectance infrared Fourier transform spectroscopy.

Taking $NiMn_2O_4$ as an example, we investigated the oxidation mechanism of C_3H_8 by *in situ* DRIFTS. The adsorption spectra of C_3H_8 over $NiMn_2O_4$ at 50 °C are shown in Figure 7. During the 30 min adsorption process, the characteristic peaks of adsorbed C_3H_8 slightly intensified and then remained constant, indicating that adsorption saturation was reached. After C_3H_8 adsorption, distinct bands appeared at 2,860-3,000 cm^{-1} and were assigned to asymmetric stretching of -CH_3 and -CH_2 groups[56], confirming the adsorption of gaseous C_3H_8. The 1,198 and 1,248 cm^{-1} bands were attributed to C-O stretching vibrations, providing evidence for dissociative C_3H_8 adsorption and the formation of surface alkoxy intermediates[35]. The absorption band at 1,501 cm^{-1} was attributed to the bending vibrations of -CH_3 and -CH_2 groups. Compared with the corresponding band in gaseous C_3H_8, this band exhibited a pronounced blue shift, suggesting that C_3H_8 molecules interacted with the catalyst surface and were initially activated. The band at 1,633 cm^{-1} was ascribed to the C=C stretching vibration of propylene, indicating that a dehydrogenation pathway to propylene existed on the catalyst[57].

O_2 was subsequently added to the feed to study C_3H_8 catalytic oxidation over the catalyst at different temperatures [Figure 7C and D]. The propylene C=C stretching band at 1,633 cm^{-1}[57] gradually weakened and eventually disappeared as the temperature increased. Concurrently, oxygen-containing intermediates appeared, including carbonate (1,342, 1,426 cm^{-1}) and carboxylate (1,578 cm^{-1}) species[58,59]. The carboxylate content initially increased and then decreased: at lower temperatures, continuous C_3H_8 oxidation generated carboxylates that accumulated on the surface, leading to an increase in band intensity. Upon further temperature elevation, the carboxylates underwent deep oxidation to CO_2 and H_2O, with the consumption rate exceeding the formation rate, resulting in a subsequent decrease in band intensity.

Based on these observations, the reaction pathway for C_3H_8 catalytic oxidation can be summarized as follows: C_3H_8 adsorption and dissociation → dehydrogenation to propylene → oxidation to carboxylates/carbonates → deep oxidation to CO_2 and H_2O. A comparative study of C_3H_8 oxidation

over different spinel catalysts was conducted at 200 and 250 °C [Figure 7A]. The types of surface-generated intermediates during C_3H_8 oxidation were similar across the catalysts. However, at 250 °C, the characteristic carboxylate peaks over $NiMn_2O_4$ decreased significantly, and $NiMn_2O_4$ showed the least accumulation of intermediates, indicating that the oxygen-containing intermediates underwent deep oxidation more effectively over this catalyst.

To further investigate the MvK mechanism in C_3H_8 oxidation, C_3H_8 oxidation experiments were performed over $^{18}O_2$-pretreated $NiMn_2O_4$, with the reaction monitored by *in situ* DRIFTS coupled with online MS. During pretreatment, the O_{latt} of the catalyst was labeled with ^{18}O at 450 °C. Signals at mass-to-charge ratios (m/z) of 18, 20, 44, 46, and 48 were monitored in real time.

Compared with the $^{16}O_2$-pretreated sample, the $^{18}O_2$-pretreated catalyst exhibited red shifts in the C-O stretching band of surface carbonate species and the asymmetric stretching band of carboxylate COO^- species [Figure 8]. For example, the band shifted from 1,576 to 1,567 cm^{-1}. This isotope-induced shift indicates that the pre-labeled ^{18}O was incorporated into surface oxygen-containing intermediates[60]. This also indicates that lattice ^{18}O participates in C_3H_8 oxidation even in the presence of gas-phase $^{16}O_2$.

MS showed that the $^{16}O_2$-pretreated reference sample primarily generated signals at m/z = 44 and 18, corresponding to CO_2 and H_2O containing ^{16}O, respectively. For the $^{18}O_2$-pretreated sample, the signals of ^{18}O-containing products (m/z = 46, 48, and 20) were weak at 150 °C, indicating a relatively low rate of lattice-^{18}O migration or participation in the reaction at this temperature. At 250 °C, the signals at m/z = 46, 48, and 20 increased markedly, demonstrating more extensive participation of lattice ^{18}O in propane oxidation. The m/z = 48 signal, assigned to $C^{18}O_2$, decreased first, followed by a gradual decline in the m/z = 46 signal, assigned to $C^{16}O^{18}O$. This behavior is consistent with the progressive consumption of pre-labeled surface ^{18}O, followed by the incorporation of gas-phase ^{16}O into the products. Meanwhile, the m/z = 44 signal, assigned to $C^{16}O_2$, initially increased and then approached a steady level. The signal of ^{18}O-containing water (m/z = 20) first increased and then decreased, whereas that of ^{16}O-containing water (m/z = 18) gradually increased. Together, the DRIFTS and isotopic MS observations indicate that C_3H_8 oxidation over $NiMn_2O_4$ follows the MvK mechanism: C_3H_8 reacts with O_{latt}, and gaseous O_2 replenishes the vacancies created by CO_2 desorption. Thus, feed O_2 mainly contributes to CO_2 formation indirectly through lattice-oxygen replenishment rather than by direct participation in the initial oxidation step.

CONCLUSIONS

In summary, this study successfully developed a series of AMn_2O_4 (A = Co, Ni, Cu, Zn) spinel catalysts and a $CeMn_2O_x$ mixed-oxide reference sample for the simultaneous catalytic elimination of NO_x and C_3H_8, and systematically elucidated the pivotal role of A-O-Mn superexchange interactions in governing the catalytic performance. Among the investigated catalysts, $NiMn_2O_4$ exhibited the best overall performance, achieving 91.4% C_3H_8 conversion and 92.8% NO_x conversion simultaneously at 220 °C, along with the highest N_2 selectivity and satisfactory resistance to SO_2.

Comprehensive experimental characterizations and DFT calculations revealed that the superior catalytic performance of $NiMn_2O_4$ originates from the Ni-O-Mn superexchange interaction, which exerts multifaceted control over the electronic structure and oxygen species. Specifically, the Ni-O-Mn superexchange induces strong orbital connectivity across the Ni-O-Mn network, enabling efficient electron transfer that stabilizes surface Mn^{4+} species and enhances Lewis acidity, thereby promoting the adsorption and activation of both NH_3 and C_3H_8. Concurrently, this superexchange interaction elevates both the Mn d-band center and the O p-band center, which weakens the Mn–O bond strength and lowers the E_{vac}, while maintaining electronically robust Mn–O bonds in the ground state. Collectively, these effects establish a highly efficient oxygen consumption-replenishment cycle that sustains the MvK mechanism with the lowest energy penalty for lattice oxygen extraction. This work provides an electronic-level understanding of the origins of A-O-Mn superexchange interactions in spinel lattices, informing the design of spinel oxides that exploit

bimetallic synergy and offering a strategy for developing high-performance spinel catalysts with tailored electronic structures for the simultaneous removal of NO_x and VOCs.

DECLARATIONS

Authors' contributions

Made substantial contributions to the conception and design of the study and performed data analysis and interpretation: Wu, J.; Ma, S.; Han, Y.; Liu, K.; Cui, Y.

Writing, review, and editing; conceptualization; methodology; supervision; and project administration: Hou, Y.; Bao, W.; Wang, J.; Huang, Z.

Availability of data and materials

All data required to support the conclusions of this paper are included in the manuscript and the Supplementary Materials. Additional data related to this paper can be obtained from the corresponding authors.

AI and AI-assisted tools statement

Not applicable.

Financial support and sponsorship

This work was financially supported by the National Natural Science Foundation of China (22472192, U23A20100), the Central Guiding Local Technology Development (YDZJSX2024D077) and the Key Research and Development Program of Shanxi Province (202302090301013, 202302090301015, 202502090301009).

Conflicts of interest

All authors declared that there are no conflicts of interest.

Ethical approval and consent to participate

Not applicable.

Consent for publication

Not applicable.

Copyright

© The Author(s) 2026.

Supplementary Materials

Supplementary Materials

REFERENCES

1. Sun, C.; Ye, L.; Lu, P.; et al. Synergistic removal of acetone and NO_x by Ag modified Mn/HZSM-5 catalyst. *Chem. Eng. J.* **2025**, *505*, 159622. DOI
2. Mi, J.; Liu, H.; Yang, S.; et al. Dual activation of molecular NO and O_2 on a Pr-doped CeO_2-TiO_2 catalyst for the simultaneous catalytic purification of NO*x* and toluene. *Environ. Sci. Technol.* **2025**, *59*, 11321-9. DOI PubMed
3. Lyulyukin, M. N.; Kolinko, P. A.; Selishchev, D. S.; Kozlov, D. V. Hygienic aspects of TiO_2-mediated photocatalytic oxidation of volatile organic compounds: air purification analysis using a total hazard index. *Appl. Catal. B:. Environ.* **2018**, *220*, 386-96. DOI
4. Liu, B.; Ji, J.; Zhang, B.; et al. Catalytic ozonation of VOCs at low temperature: a comprehensive review. *J. Hazard. Mater.* **2022**, *422*, 126847. DOI PubMed
5. Lin, B.; Guo, Z.; Tang, J.; Chen, P.; Ye, D.; Hu, Y. Modulating the microstructure and surface acidity of MnO_2 by doping-induced phase transition for simultaneous removal of toluene and NO_x at low temperature. *Environ. Sci. Technol.* **2024**, *58*, 10398-408. DOI PubMed
6. Wang, Y.; Ma, X.; Liu, H.; et al. Promoting effect of hydroxyl groups on the CO-SCR activity of Ir-Mo bimetallic catalysts under O_2 and SO_2. *Greenverse. Sci.* **2026**, *1*, 9. DOI
7. Long, Y.; Su, Y.; Xue, Y.; Wu, Z.; Weng, X. V_2O_5-WO_3/TiO_2 catalyst for efficient synergistic control of NO_x and chlorinated organics: insights into the arsenic effect. *Environ. Sci. Technol.* **2021**, *55*, 9317-25. DOI PubMed
8. Zhu, X.; Yuan, X.; Song, Z.; Peng, Y.; Li, J. A dual-balance strategy via phosphate modification on MnO_2-CeO_2 for NO_x and chlorobenzene synergistic catalytic control. *Appl. Catal. B:. Environ.* **2024**, *342*, 123364. DOI
9. Dong, C.; Yang, C.; Ren, Y.; et al. Local electron environment regulation of spinel $CoMn_2O_4$ induced effective reactant adsorption and transformation of lattice oxygen for toluene oxidation. *Environ. Sci. Technol.* **2023**, *57*, 21888-97. DOI PubMed
10. Yang, Y.; Si, W.; Peng, Y.; et al. Defect engineering on $CuMn_2O_4$ spinel surface: a new path to high-performance oxidation catalysts. *Environ. Sci. Technol.* **2022**, *56*, 16249-58. DOI PubMed
11. Zhao, L.; Yang, Y.; Liu, J. Insight into the reaction mechanism of NH_3-SCR and chlorobenzene oxidation over Mn-based spinel catalysts. *J. Hazard. Mater.* **2025**, *492*, 138113. DOI PubMed
12. Xing, X.; Li, Z.; Wang, Y.; et al. Synergistic catalytic degradation of benzene and toluene on spinel MMn_2O_4 (M Co, Ni, Cu) catalysts. *J. Environ. Sci.* **2025**, *154*, 238-51. DOI PubMed

13. Jiang, X.; Liu, Z.; Liang, J.; et al. Surface oxygen vacancy induced selective conversion of syngas to propane over ZnM_2O_4 spinel/SAPO-34 composite catalysts. *Appl. Catal. B:. Environ. Energy.* **2025**, *367*, 125126. DOI
14. Sun, Y.; Liao, H.; Wang, J.; et al. Covalency competition dominates the water oxidation structure-activity relationship on spinel oxides. *Nat. Catal.* **2020**, *3*, 554-63. DOI
15. Pan, W.; Wei, Y.; Yang, W.; Fang, D. Recent advance of spinel-based catalysts for selective catalytic reduction of NO_x. *J. Energy. Inst.* **2025**, *123*, 102301. DOI
16. Liu, R.; Jia, X.; Li, L.; et al. Regulating the Cu-Ce interaction of $CuCeO_x$/SAPO-34 catalysts to achieve a wide reaction temperature window for the collaborative synergistic removal of NO_x and toluene at low temperatures and reaction mechanisms. *J. Hazard. Mater.* **2025**, *492*, 138103. DOI PubMed
17. Gevers, L. E.; Enakonda, L. R.; Shahid, A.; et al. Unraveling the structure and role of Mn and Ce for NO_x reduction in application-relevant catalysts. *Nat. Commun.* **2022**, *13*, 2960. DOI PubMed PMC
18. Zheng, F.; Lu, J.; Chen, J.; Ren, E.; Qu, H. Bifunctional action of NaOH etching on MOFs-derived spinel $CoMn_2O_4$ for low-temperature toluene oxidation: nanoparticle disaggregation and MnO bond modulation. *Chem. Eng. J.* **2025**, *522*, 167221. DOI
19. Zhou, Y.; Sun, S.; Xi, S.; et al. Superexchange effects on oxygen reduction activity of edge-sharing $[Co_xMn_{1-x}O_6]$ octahedra in spinel oxide. *Adv. Mater.* **2018**, *30*, 1705407. DOI PubMed
20. Wu, Y.; She, T.; Wang, Y.; et al. Enhancing cationic superexchange interaction via adjustive lattice distortion in cobalt-based perovskite for improved Fenton-like decontamination. *Appl. Catal. B:. Environ.* **2024**, *343*, 123569. DOI
21. Luo, J.; Sun, S.; He, Z.; Zhu, G.; Huang, H.; Ma, R. Microwave-induced dual-responsive spinel ($Co_xMn_{1-x}Fe_2O_4$) target-triggered non-radical pathways of peroxymonosulfate: superexchange interaction and synergistic mechanism. *Appl. Catal. B:. Environ. Energy.* **2024**, *359*, 124497. DOI
22. Chen, F.; Zhao, R.; Zhao, H.; et al. Axial Co-O-Cu pairs enable superexchange interaction for efficient Co^{IV}=O formation toward water purification. *J. Am. Chem. Soc.* **2025**, *147*, 43086-97. DOI PubMed
23. Zheng, C.; Wang, Y.; Mao, H.; et al. Superexchange interaction regulates Ni/Mn spin states triggering Ni-t_{2g}/O-2p reductive coupling enabling stable lithium-rich cathode. *Nat. Commun.* **2025**, *16*, 3900. DOI PubMed PMC
24. Wu, M.; Chen, C.; Duo, J.; et al. Super-exchange interaction enables $Fe_{2-x}Mn_xO_3$ perovskite with excellent catalytic oxidation activity toward hexabromocyclododecane under humidity. *J. Hazard. Mater.* **2024**, *479*, 135691. DOI PubMed
25. Liu, X.; Ren, Z.; Zhang, Y.; et al. Deciphering the mechanistic origins of geometric-site-dependent bimetallic superexchange interactions in spinel oxides to boost VOCs catalytic oxidation. *Appl. Catal. B:. Environ. Energy.* **2026**, *381*, 125908. DOI
26. Kresse, G.; Furthmüller, J. Efficient iterative schemes for *ab initio* total-energy calculations using a plane-wave basis set. *Phys. Rev. B.* **1996**, *54*, 11169-86. DOI PubMed
27. Perdew, J. P.; Burke, K.; Ernzerhof, M. Generalized gradient approximation made simple. *Phys. Rev. Lett.* **1996**, *77*, 3865-8. DOI PubMed
28. Kresse, G.; Joubert, D. From ultrasoft pseudopotentials to the projector augmented-wave method. *Phys. Rev. B.* **1999**, *59*, 1758-75. DOI
29. Blöchl, P. E. Projector augmented-wave method. *Phys. Rev. B.* **1994**, *50*, 17953-79. DOI PubMed
30. Grimme, S.; Antony, J.; Ehrlich, S.; Krieg, H. A consistent and accurate *ab initio* parametrization of density functional dispersion correction (DFT-D) for the 94 elements H-Pu. *J. Chem. Phys.* **2010**, *132*, 154104. DOI PubMed
31. Dong, C.; Qu, Z.; Qin, Y.; Fu, Q.; Sun, H.; Duan, X. Revealing the highly catalytic performance of spinel $CoMn_2O_4$ for toluene oxidation: involvement and replenishment of oxygen species using in situ designed-TP techniques. *ACS. Catal.* **2019**, *9*, 6698-710. DOI
32. Guo, Z. Y.; Li, C. X.; Gao, M.; et al. Mn-O covalency governs the intrinsic activity of Co-Mn spinel oxides for boosted peroxymonosulfate activation. *Angew. Chem. Int. Ed. Engl.* **2021**, *60*, 274-80. DOI PubMed
33. Ma, S.; Hou, Y.; Yang, Y.; et al. Mechanism of SO_2 effect on the simultaneous removal of NO_x and propane over bifunctional $NiMn_2O_4$-CeO_2 catalysts. *J. Hazard. Mater.* **2024**, *480*, 136473. DOI PubMed
34. Hou, S.; Fang, D.; Li, Q.; et al. Structure and activity relationships of AMn_2O_4 (A = Mg and Zn) spinels in selective catalytic reduction of NO_x with NH_3. *Sep. Purif. Technol.* **2024**, *345*, 127230. DOI
35. Ma, S.; Hou, Y.; Li, Y.; et al. Regulation of A-site cations in AMn_2O_x spinel catalysts on the deep oxidation of light alkanes VOCs. *Fuel* **2023**, *334*, 126785. DOI
36. Wang, X. T.; Ouyang, T.; Wang, L.; Zhong, J. H.; Ma, T.; Liu, Z. Q. Redox-inert Fe^{3+} ions in octahedral sites of Co-Fe spinel oxides with enhanced oxygen catalytic activity for rechargeable zinc-air batteries. *Angew. Chem. Int. Ed. Engl.* **2019**, *58*, 13291-6. DOI PubMed
37. Gu, W.; Li, C.; Qiu, J.; Yao, J. Facile fabrication of flower-like MnO_2 hollow microspheres as high-performance catalysts for toluene oxidation. *J. Hazard. Mater.* **2021**, *408*, 124458. DOI PubMed
38. Aadil, M.; Taki, A. G.; Zulfiqar, S.; et al. Gadolinium doped zinc ferrite nanoarchitecture reinforced with a carbonaceous matrix: a novel hybrid material for next-generation flexible capacitors. *RSC. Adv.* **2023**, *13*, 28063-75. DOI PubMed PMC

39. Wang, X.; Zhou, X.; Hua, M.; et al. Recent advances in the strategies of developing water-resistant catalysts for the removal of atmospheric pollutants. *Greenverse. Sci.* **2026**, *1*, 15. DOI
40. Li, K.; Li, T.; Dai, Y.; Quan, Y.; Zhao, J.; Ren, J. Highly active urchin-like MCo_2O_4 (M = Co, Cu, Ni or Zn) spinel for toluene catalytic combustion. *Fuel* **2022**, *318*, 123648. DOI
41. Biesinger, M. C.; Payne, B. P.; Grosvenor, A. P.; Lau, L. W.; Gerson, A. R.; Smart, R. S. Resolving surface chemical states in XPS analysis of first row transition metals, oxides and hydroxides: Cr, Mn, Fe, Co and Ni. *Appl. Surf. Sci.* **2011**, *257*, 2717-30. DOI
42. Feng, C.; Xiong, G.; Jiang, F.; et al. Assembly of sphere-structured MnO_2 for total oxidation of propane: structure-activity relationship and reaction mechanism determination. *Sep. Purif. Technol.* **2022**, *284*, 120269. DOI
43. Wang, Y.; Bi, Y.; Ji, G.; et al. Acid-activated α-MnO_2 for photothermal co-catalytic oxidative degradation of propane: activity and reaction mechanism. *J. Hazard. Mater.* **2024**, *478*, 135447. DOI PubMed
44. Shan, C.; Zhang, Y.; Zhao, Q.; et al. New insight into opposite oxidation behavior in acetone and propane catalytic oxidation over CoMn based spinel oxides. *Chem. Eng. J.* **2023**, *476*, 146550. DOI
45. Shadravan, V.; Bukas, V. J.; Gunasooriya, G. T. K. K.; et al. Effect of manganese on the selective catalytic hydrogenation of CO_x in the presence of light hydrocarbons over Ni/Al_2O_3: an experimental and computational study. *ACS. Catal.* **2020**, *10*, 1535-47. DOI
46. Qin, Y.; Fan, S.; Gao, J.; Tadé, M. O.; Liu, S.; Li, X. Effect of Cu-doped Co-Mn spinel for boosting low-temperature NO reduction by CO: exploring the structural properties, performance, and mechanisms. *ACS. Appl. Mater. Interfaces.* **2023**, *15*, 11885-94. DOI PubMed
47. Lu, S.; Guo, X.; Xu, X.; et al. POM-promoted synergistic catalysis of NO and chlorobenzene over amorphous MnCeOx catalysts: activation of lattice oxygen, role of acid site, catalytic mechanism. *J. Hazard. Mater.* **2025**, *495*, 138873. DOI PubMed
48. Kang, D.; Shi, Q.; Zhang, C.; et al. Synergistic removal of NO_x and CB by Co-MnO_x catalysts in a low-temperature window. *Chem. Eng. J.* **2023**, *476*, 146369. DOI
49. Xu, W.; Chen, X.; Chen, J.; Jia, H. Bimetal oxide CuO/Co_3O_4 derived from Cu ions partly-substituted framework of ZIF-67 for toluene catalytic oxidation. *J. Hazard. Mater.* **2021**, *403*, 123869. DOI PubMed
50. Deng, Y.; Shang, Y.; Huang, T.; et al. Reversing the HCl/Cl_2 selectivity for efficient catalytic elimination of dichloromethane by incorporation of Ti^{4+} into CeO_2 lattice. *Appl. Catal. B:. Environ. Energy.* **2025**, *373*, 125338. DOI
51. Zhou, Y.; Sun, S.; Wei, C.; et al. Significance of engineering the octahedral units to promote the oxygen evolution reaction of spinel oxides. *Adv. Mater.* **2019**, *31*, e1902509. DOI PubMed
52. Chu, P.; Zhang, L.; Wang, Z.; et al. Regulation lattice oxygen mobility via dual single atoms for simultaneously enhancing VOC oxidation and NO_x reduction. *Environ. Sci. Technol.* **2024**, *58*, 17475-84. DOI PubMed
53. Liu, J.; Li, X.; Zhao, Q.; et al. Mechanistic investigation of the enhanced NH3-SCR on cobalt-decorated Ce-Ti mixed oxide: *in situ* FTIR analysis for structure-activity correlation. *Appl. Catal. B:. Environ.* **2017**, *200*, 297-308. DOI
54. Wang, M.; Naman, N.; Shen, Y.; et al. Synergistic catalytic removal of NO_x and chlorinated aromatics via atomically dispersed asymmetric Mn-O-Ce sites on montmorillonite. *Appl. Catal. B:. Environ. Energy.* **2025**, *378*, 125594. DOI
55. Liu, Z.; Liu, H.; Feng, X.; Ma, L.; Cao, X.; Wang, B. Ni-Ce-Ti as a superior catalyst for the selective catalytic reduction of NO_x with NH_3. *Mol. Catal.* **2018**, *445*, 179-86. DOI
56. Wu, S.; Feng, C.; Dong, F.; et al. Tailored $CoNiO_x$@$CuVO_x$ core-shell catalyst exhibiting strong charge transfer and SO_2 tolerance for efficient elimination of propane. *Appl. Catal. B:. Environ. Energy.* **2025**, *372*, 125293. DOI
57. Li, G.; Li, N.; Sun, Y.; et al. Efficient defect engineering in Co-Mn binary oxides for low-temperature propane oxidation. *Appl. Catal. B:. Environ.* **2021**, *282*, 119512. DOI
58. Zhu, W.; Li, Y.; Liu, H.; Yan, Y.; Liang, C. Boosting catalytic oxidation of propane over CeO_2-supported Co_3O_4 catalyst with strong interfacial interaction and electron transfer. *J. Catal.* **2024**, *434*, 115529. DOI
59. Du, S.; Hu, J.; Peng, D.; et al. Simultaneous removal of ethane and NO_x over Ce-MnO_2 catalysts: insights into dual-functional mechanisms and temperature-dependent interactions. *J. Catal.* **2025**, *450*, 116281. DOI
60. Ren, Z.; Wu, Z.; Song, W.; et al. Low temperature propane oxidation over Co_3O_4 based nano-array catalysts: Ni dopant effect, reaction mechanism and structural stability. *Appl. Catal. B:. Environ.* **2016**, *180*, 150-60. DOI

Disclaimer/Publisher's Note: All statements, opinions, and data contained in this publication are solely those of the individual author(s) and contributor(s) and do not necessarily reflect those of OAE and/or the editor(s). OAE and/or the editor(s) disclaim any responsibility for harm to persons or property resulting from the use of any ideas, methods, instructions, or products mentioned in the content.



© The Author(s) 2026. Open Access This article is licensed under a Creative Commons Attribution 4.0

International License (https://creativecommons.org/licenses/by/4.0/), which permits unrestricted use, sharing, adaptation, distribution and reproduction in any medium or format, for any purpose, even commercially, as long as you give appropriate credit to the original author(s) and the source, provide a link to the Creative Commons license, and indicate if changes were made.